Magnetism control with enhanced hard magnetic temperature in heterostructures based on the van der Waals magnet Fe_5GeTe_2

Chunsheng Wang,[1,*] Kejia Zhu,[1,*] Yupeng Ma,[1,*] Longyu Lu,[2] Tao Hu,[2] Liang Li,[3] Xucai Kan,[2] Yimin Xiong,[1,4] Yingying Zhang,[5,†] Guopeng Wang,[1,‡] Zhengcao Li,[5] and Mingliang Tian[1,§]

[1]*School of Physics and Optoelectronics Engineering, Anhui University, Hefei 230601, China*

[2]*School of Materials Science and Engineering, Anhui University, Hefei 230601, China*

[3]*Key Laboratory of Materials Physics, Anhui Key Laboratory of Nanomaterials and Nanotechnology, Institute of Solid State Physics, Hefei Institutes of Physical Science, Chinese Academy of Sciences, Hefei 230031, China*

[4]*Hefei National Laboratory, Hefei 230028, China*

[5]*State Key Laboratory for New Ceramics and Fine Processing, Key Laboratory of Advanced Materials of Ministry of Education, School of Materials Science and Engineering, Tsinghua University, Beijing 100084, China*

(Received 13 April 2023; revised 1 August 2023; accepted 14 August 2023; published 5 September 2023)

The discovery of two-dimensional magnets with intrinsic ferromagnetic or antiferromagnetic orders has opened up promising prospects for exploring magnetism at the desired thickness, paving the way for novel spintronic applications. In practice, the manipulation of the magnetic state in van der Waals ferromagnets is highly demanding but remains a significant challenge. In this work, we demonstrate that the magnetic states of the Fe_5GeTe_2 (FGT)-based heterostructures can be substantially tuned through a natural oxidation process. During this process, the exchange bias effect is observed in the naturally oxidized FGT flakes, confirming the existence of exchange coupling between the ferromagnetic FGT layer and antiferromagnetic oxide layer. Through the exchange coupling, the formed oxide layer affects the magnetic ordering of the Fe1 sites and magnetic anisotropy, which is evidenced by the increment of hard magnetic temperature. Theoretical calculations shed light on the crucial role of the oxide layer in the magnetic state transitions. These results provide valuable insights into the understanding and manipulation of the emergent magnetic states, leading to significant advances in the realization of practical two-dimensional spintronics.

DOI: 10.1103/PhysRevB.108.094408

I. INTRODUCTION

The emergence of intrinsic magnetism in two-dimensional (2D) van der Waals (vdW) materials has promoted rapid development in information memory, spintronics, and magnetoelectrics [1–5]. Moreover, the development of appealing artificial heterostructures based on 2D vdW magnets provides a unique platform for exploring the exotic physical properties and potential applications [6–8]. Typically, artificial heterostructures are constructed by vertically stacking various exfoliated vdW materials, exhibiting merits of high-quality interfaces between different materials, controllable thickness of the devices, and the flexibility to create variable stacking configurations [9–11]. In addition, chemical-vapor deposition and molecular beam epitaxy provide alternative ways for growing highly uniform and crystalline quality heterostructures [12,13]. Taking advantage of these advanced techniques, intriguing phenomena such as the magnetic proximity effect, spin-orbit torque, superconductivity, and quantum anomalous Hall effect have been extensively investigated [14–20]. However, the yield and reproducibility of these approaches are fundamentally constrained by the complex fabrication processes, valuable instruments, and intricate manufacturing techniques. Consequently, these methods are time-consuming and not industrially scalable. Hence, an alternative easy and versatile strategy is urgently needed to develop novel vdW heterostructures.

Since the first discovery of exchange interaction between antiferromagnetic (AFM) and ferromagnetic (FM) materials, the effect has found wide application in spintronic devices for data storage [21,22]. Through the exchange coupling, the FM spins are unidirectionally pinned by the AFM, leading to the emergence of the exchange bias (EB) effect and an increase in the coercive field (H_C). In addition to traditional FM/AFM thin films and core/shell systems, the exchange coupling has also been investigated in various 2D vdW FM/AFM systems, benefiting from the rapid growth of 2D vdW magnets [11,23–27]. For cases such as the $Fe_3GeTe_2/FePS_3$ heterostructure, the proximity coupling enhanced the coercive field and EB effect has been observed [24]. This finding is significant for Fe_3GeTe_2, which possesses a hard magnetic phase, making it a promising building block for heterostructure-based spintronics [28]. In addition, the hard magnetic phase would possess more significant potential for applications if it could exist at high temperatures. In contrast to artificially stacked heterostructures, several works have reported robust and tunable EB in naturally oxidized Fe_3GeTe_2-based flakes or heterostructures, in which the oxide layer is hypothesized

*These authors contributed equally to this work.
†Corresponding author: 20239@ahu.edu.cn
‡Corresponding author: zyy2023@tsinghua.edu.cn
§Corresponding author: mltian@ahu.edu.cn

to present an AFM state [24,27,29]. Nevertheless, the precise chemical composition and magnetic nature of the oxide phase as well as its correlation with interface coupling remain elusive. Furthermore, previous researches are mainly focused on the EB effect, while the tuning of the intrinsic magnetic ground state during the oxidation process has been rarely reported. Given the easily oxidized nature of Fe_nGeTe_2 ($n = 3,\ 4,\ 5$) when exposed to air, it is crucial to pay more attention to the interface coupling and investigate its impact on magnetic properties [29]. Despite the above open questions, the oxidized strategy is actually an easy and effective method for creating 2D vdW ferromagnet-based heterostructures and manipulating the magnetic properties.

Among the family of Fe_nGeTe_2 ($n = 3,\ 4,\ 5$), Fe_5GeTe_2 (FGT) is a Stoner-type itinerant ferromagnet with a space group $\bar{R}3m$, which is noteworthy due to its high Curie temperature (T_C) [30–34]. In this study, we propose a facile and efficient oxidized tactic to manipulate the magnetic states through the formation of FGT-based heterostructures. During this oxidation process, the exchange coupling between the oxide layer and FGT layer leads to the modulation of the magnetic states, specifically at the Fe1 site. Furthermore, the magnetic anisotropy can be controlled, as confirmed by the hard magnetic temperature gradually increasing from 160 to 260 K. These observations on the control of magnetic ordering provide an efficient strategy for the advancement of spin devices based on 2D vdW ferromagnets.

II. EXPERIMENTAL

A. Sample growth and characterizations

The typical chemical vapor transport (CVT) method was employed to grow high-quality single crystals. A mixture of Fe (99.95%), Ge (99.999%), and Te (99.999%) powders with a stoichiometric ratio of 5:1:2 and iodine powder (I_2, 5 mg/cm^3) as vapor transport agent were loaded into a 20-cm-long quartz tube. The tube was then evacuated, sealed, and heated in a double temperature zone tubular furnace. After a heating process at 650–800 °C for 10 days followed by annealing in air, centimeter-sized single crystals were obtained in the tube regions of low temperature. The crystalline structure of the FGT was characterized using a room-temperature Rigaku 4-circle x-ray diffraction (XRD) diffractometer and HAADF-STEM imaging with EDS mapping in a spherical aberration-corrected (Cs-corrected) 300-kV FEI Titan G2 microscope equipped with a Super-X detector. A focused ion beam (FEI Helios Nanolab 600i) was used during the preparation of STEM samples. X-ray photoelectron spectroscopy (XPS) analyses were performed using a Thermo ESCALAB 250Xi. The Fe *L*-edge XAS spectra were carried out at the beamline BL-12B-a of the National Synchrotron Radiation Laboratory (NSRL). Total-electron-yield (TEY) mode was used to probe the sample. The DC magnetic properties were probed with a Quantum Design magnetic properties measurement system (MPMS). The temperature-dependent magnetization was measured during the warm process with an applied magnetic field of $H = 0.01$ T. Raman spectra were obtained by Raman system (FST2-Ahdx-DZ) equipped with a 532 nm laser source. The thickness was measured by the atomic force microscopy (AFM, NX10, Park).

B. Device fabrication and magneto-transport measurements

A standard Hall bar electrode of Cr/Au (3/6 nm) was patterned on a SiO_2/Si substrate using standard electron-beam lithography and metal evaporation procedures. The FGT flakes were exfoliated onto polydimethylsiloxane (PDMS) and carefully transferred onto the prepatterned Hall bar structure. All the exfoliation and transfer processes were performed inside an Ar-filled glove box (H_2O, $O_2 < 0.1$ ppm) to prevent any degradation. The device was mounted into a customer-designed puck, which was sealed with vacuum grease in the glove box. For the oxidized FGT, after the exfoliation, the flakes were instantly annealed in air at 120 °C for either 15 or 30 min to facilitate the oxide layer. Subsequently, the whole device was immediately loaded into a commercial Quantum Design physical property measurement system (PPMS) for the electrical transport measurements. To conduct the EB measurements, the temperature was initially raised to 300 K and then field cooled under a constant magnetic field. In the measurements, the magnetic field orientation was perpendicular to the sample surface. The longitudinal magnetoresistance was negligible compared to the R_{xy}, and thus we utilized the same data-processing approach as in previous work [25].

C. Density functional theory calculations

The first-principles calculations were conducted based on density functional theory (DFT) within the generalized gradient approximation (GGA) and Perdew-Burke-Ernzerhof (PBE) exchange-correlation functional, using the Vienna *ab initio* simulation package (VASP) code [35,36]. The projector-augmented-wave (PAW) method was employed to describe electron-ion interactions [37]. The energy cutoff of the plane-wave basis was set to 500 eV. A vacuum space of 20 Å was added to avoid interactions between adjacent layers. During geometry optimization, the Brillouin zone integration was performed over a Γ-centered *k*-point mesh of $12 \times 12 \times 1$ to keep the energy converged within 10^{-7} eV. Within the PBE + U framework, the effective U value of 4.3 eV was included to remove self-interaction errors. The magnetic anisotropy energy (MAE) is defined as $\mathrm{MAE} = E_{//} - E_{\perp}$, where $E_{//}$ and $E_{\perp}$ are the total energies of states parallel and perpendicular to the basal plane, respectively. MAE calculations were performed by considering the spin-orbit coupling (SOC) effect, with a *k*-point mesh of $24 \times 24 \times 1$. Correction for vdW interactions was included by the DFT-D3 method with Becke-Johnson damping function [38].

III. RESULTS AND DISCUSSION

Figure 1(a) and Fig. S1 in the Supplemental Material [39] provide a geometric representation of the FGT structure, where similar blocks of thick Fe-Ge slabs sandwiched by Te layers are observed. Specifically within each unit cell, there are nonequivalent Fe sites labeled as Fe1, Fe2, and Fe3, leading to a complex magnetic structure. Prior to fabricating the oxidized FGT (FGT-O), high-quality FGT crystals are successfully synthesized using a chemical vapor transport method [33]. The quality of the crystal is verified by the distinct vdW gaps between the FGT sublayers, the large area of the crystal, and the presence of only (0 0 *l*) Bragg peaks

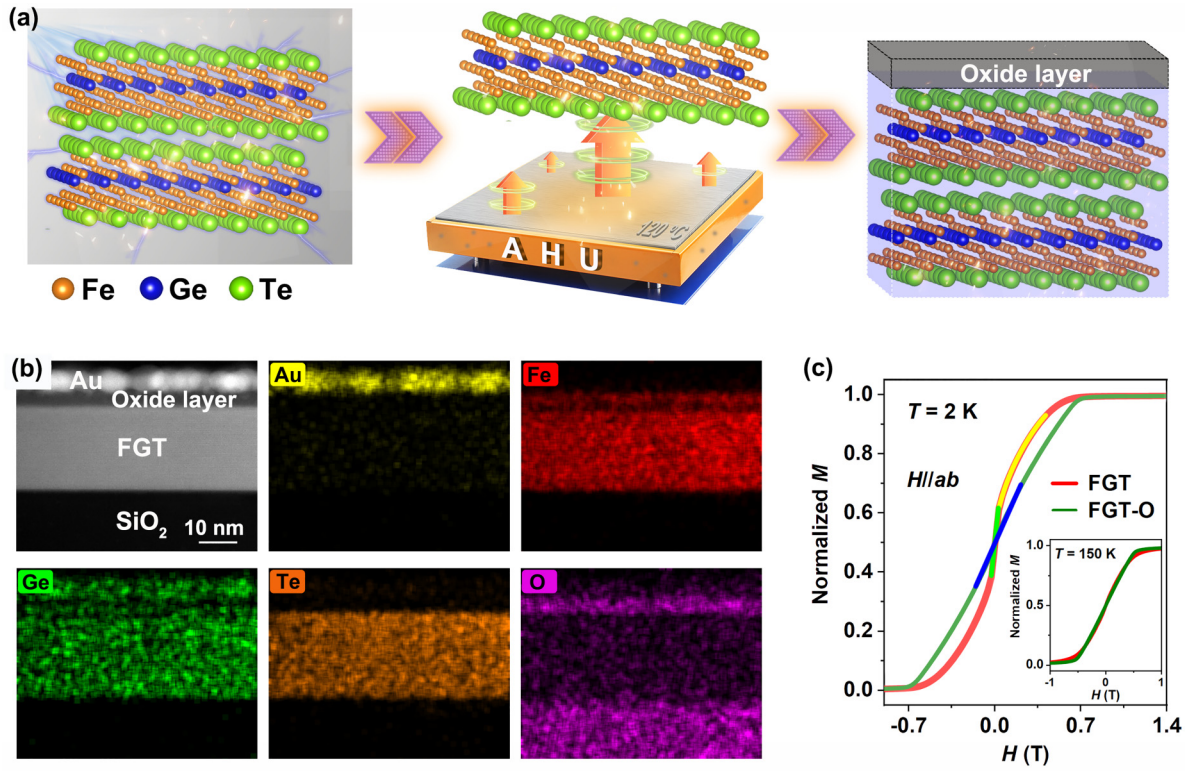

FIG. 1. (a) Schematic illustration of the FGT oxidation process. (b) Cross-sectional HAADF-STEM image and the corresponding EDS elemental mapping of oxidized FGT (FGT-O) flakes with a gold passivation layer. From the STEM image, the thickness of the oxide layer (the region between the FGT and gold layer) is about 4 nm. (c) Normalized in-plane magnetization as a function of magnetic field (H//ab) for the FGT and oxidized FGT-O crystals at $T = 2$ K and $T = 150$ K (inset).

[see Fig. S1(b) and Fig. S2 [39]]. To explore the structural transformation during the oxidation process, XRD measurements of both FGT and FGT-O bulk crystals are conducted, as shown in Fig. S2(b). Upon annealing in air at 120 °C for 48 h, the α-Fe_2O_3 phase in the FGT-O bulk crystal is clearly observed. The microscopic nature of the oxide layer can be further confirmed by the x-ray photoelectron spectroscopy (XPS) measurements, in which a higher content of Fe^{3+} is detected in the FGT-O bulk crystal compared to that of FGT (see Fig. S3 and Table S1 [39]). Moreover, by comparing the small shoulder around 707.3 eV in the Fe L edge, we observe that the local bonding and valance state of the oxide layer are similar to that of α-Fe_2O_3, suggesting the absence of ferrimagnetism Fe_3O_4 or γ-Fe_2O_3. To elucidate the origin of the phase transformation, a cross-sectional HAADF-STEM image and the corresponding EDS elemental mapping are carried out on an FGT-O flakes. Here the oxidized FGT flakes are prepared by annealing freshly cleaved FGT flakes in air at 120 °C for 30 min. The presence of a thin surface oxide layer (∼4 nm) is confirmed through the HAADF-STEM image and corresponding EDS elemental mapping. Further analysis reveals a notable reduced concentration of Te elements within the oxide layer, indicating a higher propensity for the formation of iron oxide during the oxidation process.

To gain a comprehensive understanding of the tunable magnetic state, we conduct an analysis of the temperature-dependent magnetization (M-T) of the FGT and FGT-O bulk crystals [see Fig. S4(a) [39]]. Similarly, the FGT bulk crystal exhibits much larger magnetization along the in-plane (IP, H//ab) direction with two distinct temperature kinks ($T_1 \sim 107$ K and $T_2 \sim 277$ K) [30]. Upon oxidation, two distinct characteristics concerning the fundamental properties of FGT crystal need to be addressed. First, a significant reduction in magnetization is observed, indicating the AFM nature of the oxide layer. Second, linear decreased magnetization is observed at the temperatures below $T_1 \sim 107$ K, which is in contrast to the dome-shaped magnetic behavior exhibited in the FGT bulk crystal. In the FGT bulk crystal, this anomalous magnetic transition below $T_1 \sim 107$ K is associated with the magneto-structure transition of the Fe1 site [30,31], suggesting a modulated Fe1 site after the oxidation. Isothermal magnetization (M-H) measurements provide valuable insights for determining the magnetization transition [see Figs. S4(b)–S4(f) [39]]. The M-H loops along the IP and out-of-plane (OP, H//c) directions indicate the magnetic moments prefer to align along the IP direction, which is in good agreement with the M-T data. It is noteworthy that M-H (IP) loops exhibit more intricate magnetic behaviors at a temperature below 100 K. Figure 1(c) shows the normalized M-H (IP) curves of FGT and FGT-O bulk crystals at $T = 2$ K. For the FGT bulk crystal, we can see two distinct slopes of M-H curve, with a steep slope at a low magnetic field (green curve), followed by a gradual decrease in slope until reaching saturation (yellow curve). However, for the FGT-O bulk crystal, only one slope of M-H curves is observed (blue curve). The remarkably contrasting behavior of M-H persists up to $T = 100$ K, above which the normalized M-H of FGT and FGT-O bulk crystals are almost identical [Fig. 1(c) and Fig. S4 [39]]. Such behavior

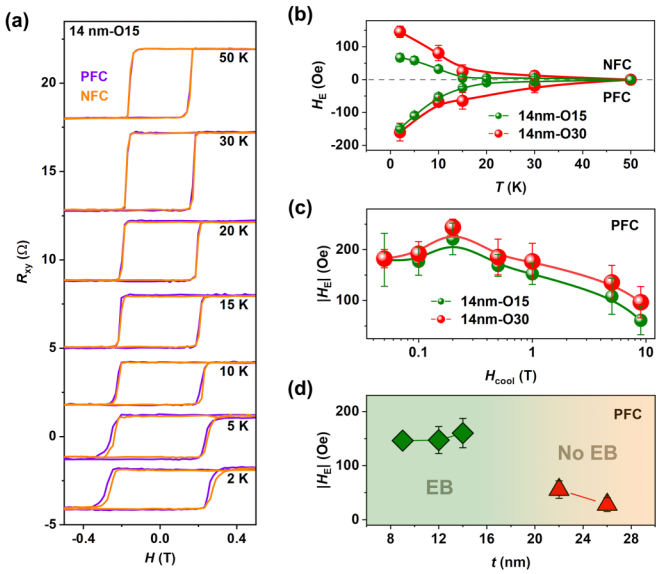

FIG. 2. EB effect in oxidized FGT flakes. (a) Anomalous Hall resistance (R_{xy}) as a function of an external magnetic field for 14 nm-O15 flake under positive (PFC, $H_{cool} = 9$ T) and negative cooling field (NFC, $H_{cool} = -9$ T). (b) EB field (H_E) as a function of temperature for 14 nm-O15 and 14 nm-O30 flakes. (c) Cooling field H_{cool} (PFC) dependence of $|H_E|$ for 14 nm-O15 and 14 nm-O30 flakes measured at $T = 2$ K. (d) Thickness-dependent $|H_E|$ for FGT annealed with 30 min under PFC. The green square region represents the presence of EB in the oxidized FGT with the thickness $\leqslant 14$ nm, and the red triangle region represents the absence of EB (No EB) in thicker oxidized FGT flakes.

implies that the oxide layer affects the magnetic ordering of the Fe1 sites through the exchange coupling, as the steep slope may be associated with the coupling between the lattice to magnetism at $T_1 \sim 107$ K [31].

To investigate the exchange coupling between the oxide layer and FGT layer, we study the EB effect of the exfoliated thin flakes. For the formation of the oxide layer, x nm-thick freshly cleaved FGT flakes are naturally oxidized by annealing in air at 120 °C for y min (labeled as x nm-Oy). The oxide layer can be detected by the optical images [see Fig. S5(b) [39]], as the FGT flake gradually becomes invisible with increasing annealing time. During oxidation process, Raman peak of the fresh FGT flake initially located at 155 cm^{-1} splits into two separate peaks located at 129 cm^{-1} and 145 cm^{-1}, verifying the oxidized transition of FGT flakes (see Fig. S6 [39]) [31]. After fully oxidized, the FGT flake undergoes a complete transformation and turns into a highly insulating state [see Fig. S5(c) [39]]. Generally, the Hall resistance of a ferromagnetic material can be separated into two parts:

$$R_{xy} = R_H + R_{AH} = R_0 B_z + R_s M_z,$$

where the R_H is the ordinary Hall resistance and R_{AH} is the anomalous Hall resistance, which is proportional to the perpendicular magnetic M_z. R_0 and R_s are the coefficients of R_H and R_{AH}, respectively. Due to the metallic behavior of FGT, the R_H is extremely small in comparison to the anomalous Hall resistance R_{AH}. Thus, we use R_{xy} to present magnetization. As depicted in Fig. 2(a) and Fig. S7 [39], the EB effect of 14 nm-O15 and 14 nm-O30 flakes is carried out at various temperatures. The R_{xy}-H loops obtained at low temperatures exhibit a shift in the opposite direction of the cooling field, proving the existence of the EB effect in our system. The absolute EB field $|H_E|$, reaches ∼149 Oe in the 14 nm-O15 flake and ∼160 Oe in the 14 nm-O30 flake at $T = 2$ K. The H_E is extracted from the loops using the definition $H_E = (H_{C+} + H_{C-})/2$, where H_{C+} and H_{C-} represent the H_C at positive and negative fields, respectively. The H_E is relatively small but still comparable to values obtained from other heterostructures such as $Fe_3GeTe_2/MnPS(Se)_3$, $Fe_3GeTe_2/CrOCl$, and $FePS_3/Fe_5GeTe_2$ [25,32,40]. With increasing temperature, the $|H_E|$ of the 14 nm-O15 and 14 nm-30 flakes is gradually suppressed and eventually disappears above the block temperate ($T_B \sim 15$ K) due to the thermal fluctuations, as shown in Fig. 2(b). Additionally, we observe that the R_{xy}-H loops exhibit an asymmetric shift under PFC and NFC, with this behavior being more pronounced in the case of 14 nm-O15 flakes. The field-cooled process prior to the R_{xy}-H measurements is a key factor in determining the EB in oxidized FGT flakes. Notably, the $|H_E|$ exhibits a sharp increase initially as H_{cool} reaches to 0.2 T, but subsequently decreases with further increasing H_{cool}, implying that a relatively small H_{cool} favors a large H_E [Fig. 2(c) and Fig. S8 [39]. Figure 2(d) and Fig. S9 [39] show the dependence of $|H_E|$ on the thickness t of the FGT flakes. The EB effect is observed in the oxidized FGT with the thickness $\leqslant 14$ nm. However, when the thickness of FGT $\geqslant 22$ nm, there is no detectable EB observed. From the above results, the emergence of the EB effect confirms the strong magnetic coupling between the oxide layer and FGT, highlighting the tunability of the magnetic states by the AFM oxide layer.

After establishment of the exchange coupling, we further explore the modulation of Fe1 site and magnetic states by the AFM oxide layer. Figure S10 [39] shows the normalized longitudinal resistance (R_{xx}) curves measured in FGT and oxidized FGT flakes. For the pristine flakes, R_{xx} drops with decreasing temperature and exhibit a kink at $T_R \sim 120$ K in the R_{xx}-T curve. This temperature is close to the T_1 obtained from the M-T curves of bulk crystal. The behavior that occurs at T_1 is dominantly associated with the magnetic ordering of the Fe1 sublattice, which leads to the formation of complex domain structure above T_1 (or T_R). Consequently, the reduction in complex domain structures results in reduced electron scattering, leading to a decrease in resistance below T_R (T_1) [32–34]. As the oxidized time increases, the kink temperature T_R increases monotonically until it reaches ∼170 K. However, for the thicker FGT flakes under air annealing for 30 min (labeled as 22 nm-O30 and 32 nm-O30), the T_R displays a slight decrease with increasing thickness. Due to the formation of an oxide layer (∼4 nm, annealing for 30 min), the actual thickness of the FM layer in oxidized FGT flakes is reduced. As a guide of R_{xx}-T curves of freshly cleaved 6 nm and 11 nm FGT flakes, we can eliminate the influence of the FM layer thickness on the enhanced T_R. As mentioned above, the kink temperature T_R varies across the freshly FGT and oxidized FGT and is summarized in Fig. 3(d), validating the exchange coupling effect of the oxide layer on the Fe1 sublattice.

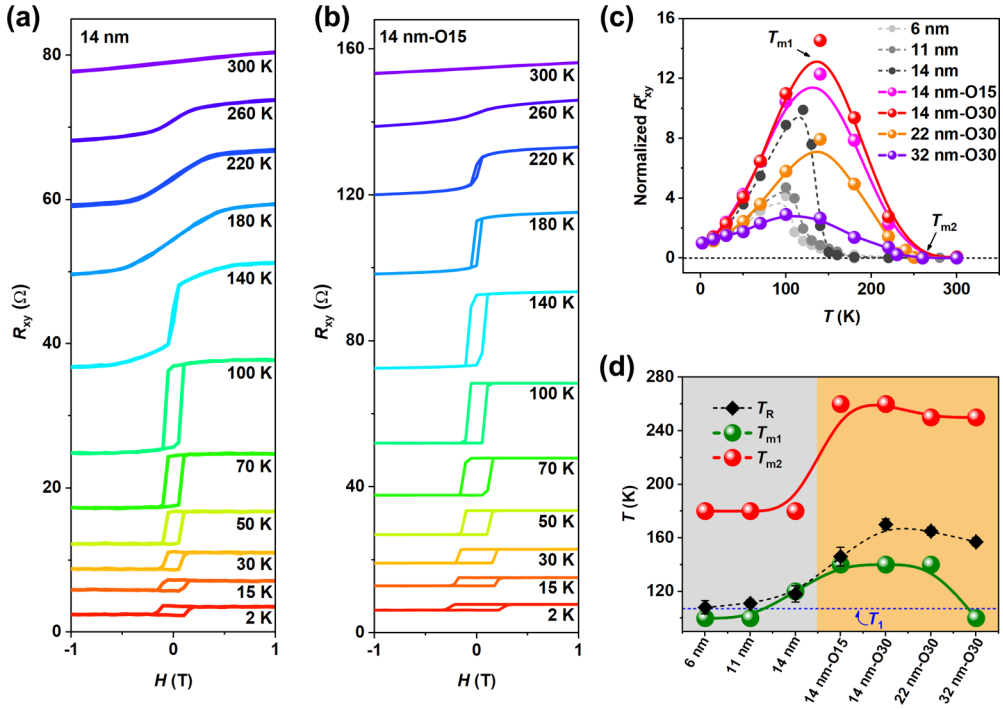

FIG. 3. Anomalous Hall effect measurements performed on FGT and oxidized FGT flakes. R_{xy} as a function of external magnetic field for the (a) 14 nm and (b) 14 nm-O15 flakes at various temperatures. (c) Remnant anomalous Hall resistance R^r_{xy} as a function of temperature obtained from FGT and oxidized FGT flakes.R^r_{xy} is normalized by its values at $T = 2$ K. The black arrows highlight magnetic transitions temperature at T_{m1} and T_{m2}. (d) T_R, T_{m1}, and T_{m2}. The blue dash line indicates the transition temperature T_1 obtained from the M-T curves of FGT bulk crystal.

To assess the viewpoint of magnetic state control through exchange coupling, we systematically measure the R_{xy} of both FGT and oxidized FGT flakes by varying the temperature and magnetic field. Figure 3(a) displays the temperature-dependent R_{xy} of the 14 nm flake from 2 to 300 K with $H//c$. A nearly square-shaped R_{xy}-H loop with $H_C \sim 0.14$ T is observed at $T = 2$ K, indicating the presence of a single hard magnetic phase. As the temperature increases, the nearly square-shaped R_{xy}-H loops gradually diminish and transition into a state with no discernible H_C or zero-field remanence features. This suggests that the FGT flakes undergo a transition from a hard FM to a soft FM state [32], which can be further characterized by temperature-dependent R^r_{xy}, as shown in Fig. 3(c). Obviously, at the hard magnetic temperature T_{m2} (defined as the existence temperature of hard magnetic phase), the R^r_{xy} shows a sudden drop to almost zero. This magnetic transition may be attributed to the spin reorientation with the magnetic easy axis changing from the out-of-plane to in-plane orientation [41]. In addition, R^r_{xy} reaches its maximum at a temperature of $\sim$120 K (denoted as T_{m1}), which is close to T_1 or T_R, implying the feature observed around T_{m1} might be related to the modulation of Fe1 sublattice. In contrast to R_{xy}-H loop of 14 nm flake, the oxidized FGT flakes exhibit similar squared-shape loops at $T = 2$ K with larger H_C [Fig. 3(b), Figs. S11 and S12 [39]]. Moreover, the R_{xy}-H of the 14 nm-O30 flake exhibits a two-step magnetic reversal transition ranging from 2 K to 50 K, which is similar to the previous report [42]. To precisely depict this phenomenon, we have deconvoluted R_{xy}-H into two distinct loops (Loop1 and Loop2), as shown in Figs. S11(b) and S11(c) [39]. It suggests that the two loops exhibit independent magnetization behavior and lack interconnection. Specifically, Loops 1 and 2 represent the R_{xy}-H of pure FGT and the oxidized FGT, respectively. In 14 nm-O15 flake, the oxide layer is very thin due to a shorter oxidized time, which has no significant impact on the overall hysteresis loops. Consequently, only the hysteresis loops of the FGT layer are observed in this scenario. To gain a deeper insight into the underlying mechanism behind the AHE, the relationship between Hall and longitudinal conductivity (σ_{xy}-σ_{xx}) of FGT and oxidized FGT are plotted, as shown in Fig. S13 [39]. The σ_{xx} value of 14 nm FGT falls near the boundary between the dirty metal and intrinsic regimes, suggesting a coexistence of both mechanisms [43–45]. Upon oxidation of the FGT flakes, we observe a shift of σ_{xy}-σ_{xx} towards the dirty metal region. This observation indicates more disorder in the oxidized flakes, which is consistent with the presence of two loops in the R_{xy}-H of oxidized FGT flake.

Moreover, with increasing oxidized time of 14 nm flake, the dome shape of the R^r_{xy}-T curves changes dramatically. Specifically, the T_{m1} value increases from 120 to 140 K and T_{m2} increases from 180 to 260 K, indicating the tunable magnetic anisotropy. In addition, when considering the same oxidized time of 30 min, both T_{m1} and T_{m2} decrease slightly with increasing the flake thickness, confirming the thickness limits for the exchange coupling. We additionally conduct R_{xy}-H measurements on freshly cleaved 6 nm and 11 nm FGT flakes for comparison, from which we can exclude the effect of FGT layer thickness on the increment of T_{m1} and T_{m2}. Based on the above analysis, the evolution of H_C as well as the variations in T_R, T_{m1}, and T_{m2} can be effectively

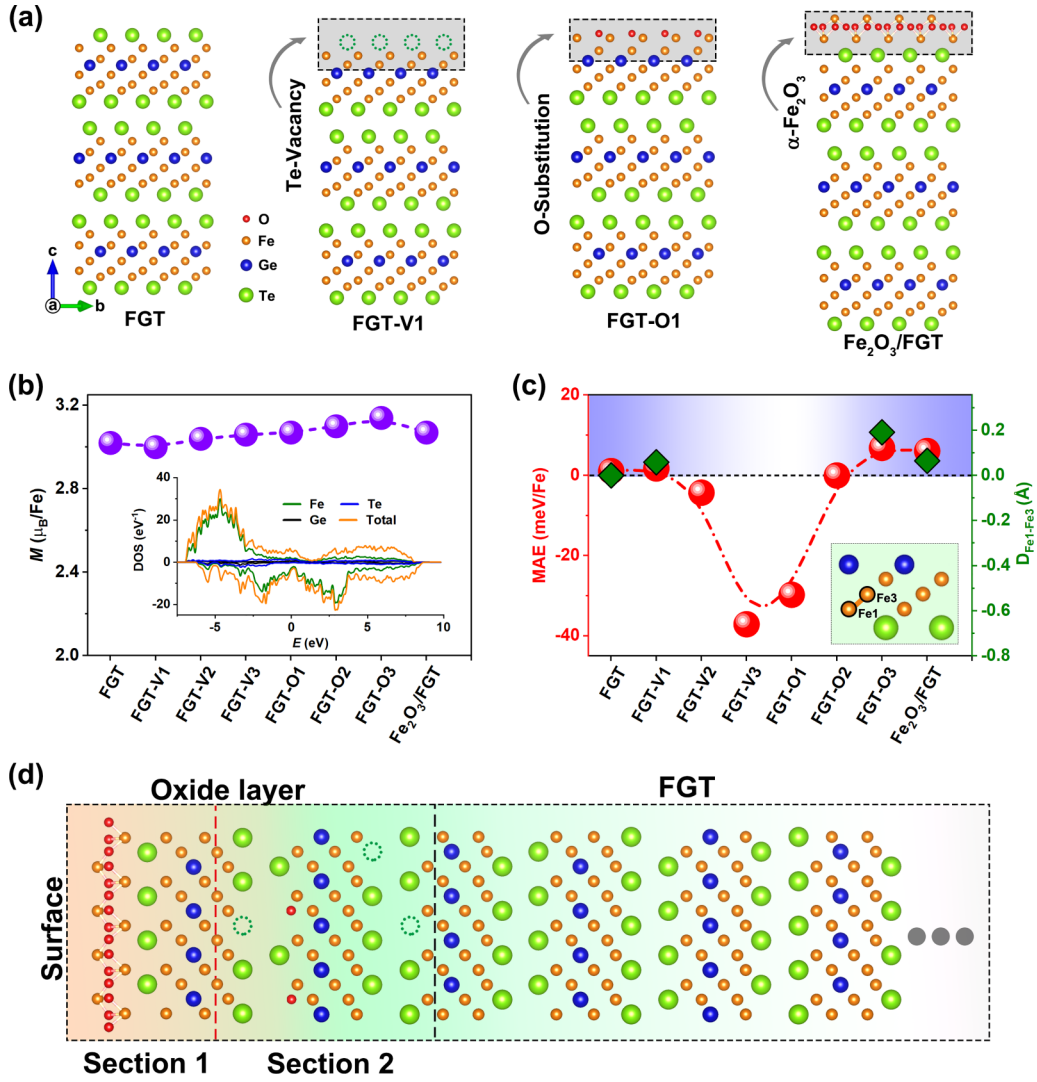

FIG. 4. First-principles calculation of FGT slab models. (a) Structural configurations of FGT, FGT-V1, FGT-O1, and Fe_2O_3/FGT slab models. FGT represents 3 uc FGT slab model. FGT-V1 and FGT-O1 represent 3 uc FGT slab models with the top tellurium atoms gone and substituted by oxygen atoms, respectively. Fe_2O_3/FGT is constructed using 1 uc Fe_2O_3 and 3 uc FGT. (b) Calculated magnetic moment for FGT and oxidized FGT. The inset is the spin-resolved density of states (DOS) of FGT around Fermi energy. (c) Calculated magnetic anisotropy energy (MAE) and bond distance of Fe1 and Fe3 ($D_{Fe1-Fe3}$) for FGT and oxidized FGT. The $D_{Fe1-Fe3}$ of FGT is set to 0 Å as a reference. The inset shows the diagram of $D_{Fe1-Fe3}$. (d) The schematic diagram of oxidation gradient along the c axis of the entire flake. The oxide layer is divided into two sections: section 1 with strong oxidation and section 2 with low oxidation.

controlled by adjusting the oxidized time and flakes thickness, as summarized in Fig. 3(d) and Figs. S12(c-d) [39], providing an opportunity for tuning the magnetic properties through the interface exchange coupling.

To gain a better understanding of the magnetic evolution during the oxidation process, we perform density functional theory (DFT) calculations. Two equivalent occupancies of Fe1 and Ge are presented as $Fe1_{down}$-Ge_{up} and $Fe1_{up}$-Ge_{down} (see Fig. S14 [39]), and having Fe1 both above and below Ge is prohibited due to the required bonding length between them [46]. In the calculation, we use the $Fe1_{down}$-Ge_{up} configuration to perform our calculations [Fig. 4(a)]. Since the H_C and spin reorientation are mainly determined by the magnetic anisotropy energy (MAE), our investigation focuses on the dependence of MAE on various oxidized FGT configurations. According to the MAE definition above, the positive MAE indicates perpendicular magnetic anisotropy (PMA). The inset of Fig. 4(b) reveals that the total density of states is mainly derived from the Fe atoms with magnetic moment $\sim 3.0\ \mu_B$/Fe. Moreover, FGT presents a positive MAE (~ 1.08 meV/Fe), consistent with the previous research [47]. Then we take into account several slab models based on the experimental results (XRD and EDS element mapping), as shown in Fig. 4(a) and Fig. S15 [39]. Figure 4(c) shows the calculated MAE of considered slab models. We find that the FGT-V1, FGT-O3, and Fe_2O_3/FGT configurations exhibit stronger MAE compared to the pristine FGT, while the calculated magnetic moments remain unchanged. Thus, the increased MAE is attributed to the variation of spin-orbit interaction rather than the unchanged spin moments, which contributes to the enhancement of H_C and T_{m2}. In the FGT, the amplitude and direction of magnetic anisotropy are affected by the interaction of d_{z^2} and d_{xz}/d_{yz}

orbitals, since the spin-minority components of these orbitals are mainly determined by spin-orbit coupling associated with the Fe sublayers [47]. To unveil the origin of MAE enhancement, we focus on FGT and Fe_2O_3/FGT as an example and decompose the calculated MAE into the coupling of Fe d_{z^2} and d_{xz}/d_{yz} pairs. In the Fe_2O_3/FGT heterostructure, the occupied d_{xz}/d_{yz} and unoccupied d_{z^2} pairs exhibit lower energy levels (see Fig. S16 [39]), resulting in the overall increment of the MAE. Intriguingly, we observe a distortion of Fe1 sublattices in the FGT-V1, FGT-O3, and Fe_2O_3/FGT configuration compared to the pristine FGT, verified by the distance between Fe1 and Fe3 sites. It is likely that the distortion contributes to the modulation of the magnetic states (M-H, T_R, and T_{m1}) induced by the oxidation process.

It is noted that 2D vdW Fe_3GeTe_2 ferromagnets, when exposed to ambient condition for a duration of up to 2 wk, undergo the formation of an oxide layer on the surface of exfoliated flakes [42]. This oxide layer exhibits an amorphous structure, and it is proposed that the O adsorbed on the bridge between the Fe and Te. In our work, we have proposed various structure configurations of oxidized FGT, taking into account the high volatility of the Te element at elevated annealing temperatures. These configurations include Te vacancies, Te atoms substituted by oxygen atoms, and the transformation of α-Fe_2O_3. In practical scenarios, different structure configurations can coexist, interconvert, or even transition into disordered spins like spin glass states, depending on the pristine FGT composition, oxidized condition, and annealing process. It is important to highlight that the interface between the oxide layer and FGT layer is not uniform enough, resulting in a considerable oxidation gradient along the c axis of the entire flakes, as verified by the presence of two distinct sections in the oxide layer (see Fig. S17 [39]). Thus, our oxide structure differs significantly from that in Fe_3GeTe_2, as the oxide layer in Fe_3GeTe_2 is solely formed through natural oxidation without any element evaporation. Drawing from these findings, we propose a distinctive structure within the oxide layer that enables the interaction between AFM (section 1 with intense oxidation) and FM (FGT layer), in conjunction with lattice distortion (as presented in section 2 with low oxidation). This configuration is believed to play a crucial role in the magnetic modulation [Fig. 4(d)].

The distinctive structure of our sample is expected to give rise to a distinct interface between the FM(FGT) and AFM (oxide layer), resulting in various FM-AFM interfaces. Under these conditions, the exchange coupling may exhibit unidirectional anisotropy under PFC and NFC processes, especially when exposed to strong thermal fluctuations at high temperature (> 2 K), resulting in the asymmetric shift in the AHE loops during the process. For 14 nm-O15 and 14 nm-O30 flakes, the thickness of the FGT layers is supposed to remain unchanged due to the thin oxide layer. As a result, the variation in the EB effect can be primarily attributed to the interface exchange coupling induced by antiferromagnetic anisotropy energy. Compared to the 14 nm-O15, the thicker oxide layer of 14 nm-O30 enhances the antiferromagnetic anisotropy energy, giving rise to stronger interface exchange coupling to pin the FM spin during magnetization reversal. This phenomenon is consistent with the conventional model of EB effect [22], leading to relatively symmetric shifts of AHE loops under PFC and NFC in 14 nm-O30 flakes.

IV. CONCLUSION

In conclusion, magnetism control is achieved in FGT-based heterostructures via a naturally oxidized strategy. We have established a full picture of electrical transport and magnetic properties by investigating oxidized time and thickness of FGT. Intrinsically enhanced T_R and T_{m1} with modulated magnetic anisotropy are achieved in the oxidized FGT. Several structure configurations are proposed with the assistance of density functional theory, and we have determined that the changeable MAE and the distorted Fe1 sublattice contribute to the magnetic state transition. Thus, we envision that the oxidation treatment provides a step toward heterostructures to modulate the magnetic state in layered vdW magnets, opening up opportunities for next-generation magnetoelectronics and spintronics.

ACKNOWLEDGMENTS

The authors want to thank the support from the Tsinghua University-Zhejiang Deqing Joint Research Center for Materials Design and Industrial Innovation. This work was financially supported by the National Natural Science Foundation of China (Grants No. 12104007 and No. U19A2093), the open fund of the Information Materials and Intelligent Sensing Laboratory of Anhui Province (Grant No. IMIS202201), the Education Department of Anhui Province (Grant No. 2022AH050081), the Innovation Program for Quantum Science and Technology (Grant No. 2021ZD0302802), and the National Key R &D Program of the MOST of China (Grant No. 2022YFA1602603).

[1] Y. J. Deng, Y. J. Yu, Y. C. Song, J. Z. Zhang, N. Z. Wang, Z. Y. Sun, Y. F. Yi, Y. Z. Wu, S. W. Wu, J. Y. Zhu *et al.*, Nature (London) **563**, 94 (2018).

[2] C. Gong, L. Li, Z. L. Li, H. W. Ji, A. Stern, Y. Xia, T. Cao, W. Bao, C. Wang, Y. Wang *et al.*, Nature (London) **546**, 265 (2017).

[3] B. Huang, G. Clark, E. Navarro-Moratalla, D. R. Klein, R. Cheng, K. L. Seyler, D. Zhong, E. Schmidgall, M. A. McGuire, D. H. Cobden *et al.*, Nature (London) **546**, 270 (2017).

[4] K. S. Burch, D. Mandrus, and J. G. Park, Nature (London) **563**, 47 (2018).

[5] J. F. Sierra, J. Fabian, R. K. Kawakami, S. Roche, and S. O. Valenzuela, Nat. Nanotechnol. **16**, 856 (2021).

[6] Y. Liu, O. W. Nathan, X. D. Duan, H. C. Cheng, Y. Huang, and X. F. Duan, Nat. Rev. Mater. **1**, 16042 (2016).

[7] K. S. Novoselov, A. Mishchenko, A. Carvalho, and N. A. H. Castro, Science **353**, 6298 (2016).

[8] M. Gibertini, M. Koperski, A. F. Morpurgo, and K. S. Novoselov, Nat. Nanotechnol. **14**, 408 (2019).

[9] W. J. Yu, Z. Li, H. L. Zhou, Y. Chen, Y. Wang, Y. Huang, and X. F. Duan, Nat. Mater. **12**, 246 (2013).

[10] C. H. Lee, G. H. Lee, A. M. van der Zande, W. C. Chen, Y. L. Li, M. Y. Han, X. Cui, G. Arefe, C. Nuckolls, T. F. Heinz *et al.*, Nat. Nanotechnol. **9**, 676 (2014).

[11] Y. Y. Wu, W. Wang, L. Pan, and K. L. Wang, Adv. Mater. **34**, 2105266 (2021).

[12] M. Y. Li, Y. M. Shi, C. C. Cheng, L. S. Lu, Y. C. Lin, H. L. Tang, M. L. Tsai, C. W. Chu, K. H. Wei, J. H. He *et al.*, Science **349**, 524 (2015).

[13] H. Y. Wang, Y. J. Liu, P. C. Wu, W. J. Hou, Y. H. Jiang, X. H. Li, C. D. Pandey, D. D. Chen, Q. Yang, H. T. Wang *et al.*, ACS Nano **14**, 10045 (2020).

[14] D. Zhong, K. L. Seyler, X. Y. Linpeng, N. P. Wilson, T. Taniguchi, K. J. Watanabe, M. A. McGuire, K. M. C. Fu, D. Xiao, Y. Wang, and X. D. Xu, Nat. Nanotechnol. **15**, 187 (2020).

[15] M. Bora and P. Deb, J. Phys. Mater. **4**, 034014 (2021).

[16] Q. M. Shao, G. Q. Yu, Y. W. Lan, Y. M. Shi, M. Y. Li, C. Zheng, X. D. Zhu, L. J. Li, P. K. Amiri, and K. L. Wang, Nano Lett. **16**, 7514 (2016).

[17] Q. L. He, H. C. Liu, M. Q. He, Y. H. Lai, H. T. He, G. Wang, K. T. Law, R. Lortz, J. N. Wang, and I. K. Sou, Nat. Commun. **5**, 4247 (2014).

[18] S. Kezilebieke, M. N. Huda, V. Vano, M. Aapro, S. C. Ganguli, O. J. Silveira, S. Glodzik, A. S. Foster, T. Ojanen, and P. Liljeroth, Nature (London) **588**, 424 (2020).

[19] X. F. Qian, J. W. Liu, L. Fu, and J. Li, Science **346**, 1344 (2014).

[20] H. X. Fu, C. X. Liu, and B. H. Yan, Sci. Adv. **6**, eaaz0948 (2019).

[21] W. H. Meiklejohn and C. P. Bean, Phys. Rev. **105**, 904 (1957).

[22] B. Diény, J. Magn. Magn. Mater. **136**, 335 (1994).

[23] R. Zhu, W. Zhang, W. Shen, P. K. J. Wong, Q. X. Wang, Q. J. Liang, Z. Tian, Y. Zhai, C. W. Qiu, and A. T. S. Wee, Nano Lett. **20**, 5030 (2020).

[24] L. M. Zhang, X. Y. Huang, H. W. Dai, M. S. Wang, H. Cheng, L. Tong, Z. Li, X. T. Han, X. Wang, L. Ye, and J. B. Han, Adv. Mater. **32**, 2002032 (2020).

[25] G. J. Hu, Y. M. Zhu, J. X. Xiang, T. Y. Yang, M. Huang, Z. Wang, Z. Wang, P. Liu, Y. Zhang, C. Feng *et al.*, ACS Nano **14**, 12037 (2020).

[26] H. W. Dai, H. Cheng, M. H. Cai, Q. H. Hao, Y. T. Xing, H. J. Chen, X. D. Chen, X. Wang, and J. B. Han, ACS Appl. Mater. Inter **13**, 24314 (2021).

[27] H. K. Gweon, S. Y. Lee, H. Y. Kwon, J. Jeong, H. J. Chang, K. W. Kim, Z. Q. Qiu, H. Ryu, C. Jang, and J. W. Choi, Nano Lett. **21**, 1672 (2021).

[28] C. Tan, J. H. Lee, S. G. Jung, T. Park, S. Albarakati, J. Partridge, M. R. Field, D. G. McCulloch, L. Wang, and C. Lee, Nat. Commun. **9**, 1554 (2018).

[29] M. H. Phan, V. Kalappattil, V. O. Jimenez, Y. T. H. Pham, N. W. Y. A. Y. Mudiyanselage, D. Delellem, C. M. Hung, A. Chanda, and T. Eggers, J. Alloys Compounds **937**, 168375 (2022).

[30] H. R. Zhang, R. Chen, K. Zhai, X. Chen, L. Caretta, X. X. Huang, R. V. Chopdekar, J. H. Cao, J. R. Sun, J. Yao *et al.*, Phys. Rev. B **102**, 064417 (2020).

[31] A. F. May, D. Ovchinnikov, Q. Zheng, R. Hermann, S. Calder, B. Huang, Z. Y. Fei, Y. H. Liu, X. D. Xu, and M. A. Mcguire, ACS Nano **13**, 4436 (2019).

[32] T. L. Zhang, Y. J. Zhang, M. Y. Huang, B. Li, Y. H. Sun, Z. Qu, X. D. Duan, C. B. Jiang, and S. X. Yang, Adv. Sci. **9**, 2105483 (2022).

[33] Y. Z. Deng, Z. J. Xiang, B. Lei, K. J. Zhu, H. M. Mu, W. H. Zhuo, X. Y. Hua, M. J. Wang, Z. F. Wang, G. P. Wang *et al.*, Nano Lett. **22**, 9839 (2022).

[34] X. C. Wu, L. Lei, Q. W. Yin, N. N. Zhao, M. Li, Z. L. Wang, Q. X. Liu, W. H. Song, H. Ma, P. F. Ding *et al.*, Phys. Rev. B **104**, 165101 (2021).

[35] J. P. Perdew, K. Burke, and M. Ernzerhof, Phys. Rev. Lett. **77**, 3865 (1996).

[36] J. Hafner, J. Comput. Chem. **29**, 2044 (2008).

[37] P. E. Blöchl, Phys. Rev. B **50**, 17953 (1994).

[38] S. Grimme, J. Antony, S. Ehrlich, and H. Krieg, J. Chem. Phys. **132**, 154104 (2010).

[39] See Supplemental Material at http://link.aps.org/supplemental/10.1103/PhysRevB.108.094408 for additional information XRD, HAADF-STEM, magnetic properties, AFM, XPS, Raman measurements, AHE, and first-principles calculations, which includes Refs. [27,43–45,48,49].

[40] S. Albarakati, W. Q. Xie, C. Tan, G. L. Zheng, M. Algarni, J. B. Li, J. Partridge, M. J. S. Spencer, L. Farrar, Y. M. Xiong *et al.*, Nano Lett. **22**, 6166 (2022).

[41] M. Tang, J. W. Huang, F. Qin, K. Zhai, T. Ideue, Z. Y. Li, F. H. Meng, A. M. Nie, L. L. Wu, X. Y. Bi *et al.*, Nat. Electron. **6**, 28 (2023).

[42] D. Kim, S. Park, J. Lee, J. Yoon, S. Joo, T. Kim, K. Min, C. Kim, S. Park, K. Moon *et al.*, Nanotechnology **30**, 245701 (2019).

[43] N. Nagaosa, J. Sinova, S. Onoda, A. H. MacDonald, and N. P. Ong, Rev. Mod. Phys. **82**, 1539 (2010).

[44] S. Onoda, N. Sugimoto, and N. Nagaosa, Phys. Rev. Lett. **97**, 126602 (2006).

[45] S. Onoda, N. Sugimoto, and N. Nagaosa, Phys. Rev. B **77**, 165103 (2008).

[46] T. T. Ly, J. Park, K. Kim, H. B. Ahn, N. J. Lee, K. Kim, T. E. Park, G. Duvjir, N. H. Lam, K. Jang *et al.*, Adv. Funct. Mater. **31**, 2009758 (2021).

[47] Q. X. Liu, J. P. Xing, Z. Jiang, Y. Guo, X. Jiang, Y. Qi, and J. J. Zhao, Commun. Phys. **5**, 140 (2021).

[48] J. S. Kang, G. Kim, H. J. Lee, D. H. Kim, H. S. Kim, J. H. Shim, S. Lee, H. Lee, J. Kim, B. H. Kim, and B. I. Min, Phys. Rev. B **77**, 035121 (2008).

[49] S. Chatterjee, J. Sau, S. Samanta, B. Ghosh, N. Kumar, M. Kumar, and K. Mandal, Phys. Rev. B **107**, 125138 (2023).